Quantifying the impact of shape uncertainty on predicted arrhythmias

Cesare Corrado [a,*], Caroline H. Roney [a,c], Orod Razeghi [a,e], Josè Alonso Solís Lemus [a], Sam Coveney [b], Iain Sim [a], Steven E. Williams [a], Mark D. O'Neill [a], Richard D. Wilkinson [d], Richard H. Clayton [b], Steven A. Niederer [a]

[a] *Division of Imaging Sciences & Biomedical Engineering, King's College London, London SE17EH, United Kingdom*
[b] *Insigneo Institute for in-silico Medicine and Department of Computer Science, University of Sheffield, Sheffield, United Kingdom*
[c] *School of Engineering and Materials Science, Queen Mary University of London, London, United Kingdom*
[d] *School of Mathematical Sciences, University of Nottingham, Nottingham, United Kingdom*
[e] *UCL Centre for Advanced Research Computing, London, United Kingdom*

ARTICLE INFO

ABSTRACT

Background. Personalised computer models are increasingly used to diagnose cardiac arrhythmias and tailor treatment. Patient-specific models of the left atrium are often derived from pre-procedural imaging of anatomy and fibrosis. These images contain noise that can affect simulation predictions. There are few computationally tractable methods for propagating uncertainties from images to clinical predictions.

Method. We describe the left atrium anatomy using our Bayesian shape model that captures anatomical uncertainty in medical images and has been validated on 63 independent clinical images. This algorithm describes the left atrium anatomy using $N_{modes} = 15$ principal components, capturing 95% of the shape variance and calculated from 70 clinical cardiac magnetic resonance (CMR) images. Latent variables encode shape uncertainty: we evaluate their posterior distribution for each new anatomy. We assume a normally distributed prior. We use the unscented transform to sample from the posterior shape distribution. For each sample, we assign the local material properties of the tissue using the projection of late gadolinium enhancement CMR (LGE-CMR) onto the anatomy to estimate local fibrosis. To test which activation patterns an atrium can sustain, we perform an arrhythmia simulation for each sample. We consider 34 possible outcomes (31 macro-re-entries, functional re-entry, atrial fibrillation, and non-sustained arrhythmia). For each sample, we determine the outcome by comparing pre- and post-ablation activation patterns following a cross-field stimulus.

Results. We create patient-specific atrial electrophysiology models of ten patients. We validate the mean and standard deviation maps from the unscented transform with the same statistics obtained with 12,000 Monte Carlo (ground truth) samples. We found discrepancies <3% and <2% for the mean and standard deviation for fibrosis burden and activation time, respectively. For each patient case, we then compare the predicted outcome from a model built on the clinical data (deterministic approach) with the probability distribution obtained from the simulated samples. We found that the deterministic approach did not predict the most likely outcome in 80% of the cases. Finally, we estimate the influence of each source of uncertainty independently. Fixing the anatomy to the posterior mean and maintaining uncertainty in fibrosis reduced the prediction of self-terminating arrhythmias from $\simeq 14\%$ to $\simeq 7\%$. Keeping the fibrosis fixed to the sample mean while retaining uncertainty in shape decreased the prediction of substrate-driven arrhythmias from $\simeq 33\%$ to $\simeq 18\%$ and increased the prediction of macro-re-entries from $\simeq 54\%$ to $\simeq 68\%$.

Conclusions. We presented a novel method for propagating shape uncertainty in atrial models through to uncertainty in numerical simulations. The algorithm takes advantage of the unscented transform to compute the output distribution of the outcomes. We validated the unscented transform as a viable sampling strategy to deal with anatomy uncertainty. We then showed that the prediction computed with a deterministic model does not always coincide with the most likely outcome. Finally, we found that shape uncertainty affects the predictions of macro-re-entries, while fibrosis uncertainty affects the predictions of functional re-entries.

---

* Corresponding author.
E-mail address: cesare.corrado@kcl.ac.uk (C. Corrado).

1. Introduction

Patient-specific models derived from clinical measurements have the potential to improve the study of heart diseases and tailor clinical treatment [1–3].

Personalised atrial pathophysiology models are routinely developed from clinical images. Magnetic resonance imaging (MRI) produces high-contrast images of atrial anatomy that can provide information on the cardiac anatomy and tissue structure for patient-specific models. In patient-specific atrial electrophysiology models, the cardiac anatomy is routinely identified using image segmentation, and then mathematically described through a meshing process. MRI images of the addition and washout of a gadolinium contrast agent allow the estimation of scar and fibrosis in the atrium [4,5]. Scar and fibrotic areas can have distinct electrical properties that affect electrical activation patterns. Estimated atria fibrosis and scar regions from late gadolinium enhancement cardiac magnetic resonance (LGE-CMR) can be used to non-invasively infer atrial electrophysiology material properties in patient-specific models.

Noise, image artefacts, and limited resolution are all factors that affect the quality of the anatomical image, introducing uncertainty in the computed anatomy, in the LGE projection, and finally in simulation results. Quantifying the uncertainty of model predictions and the data quality required to make models with sufficient accuracy to inform patient care is a fundamental step towards computer-guided medicine [6,7]. This is recognised as a critical step in the proposed V & V 40 [8] and Food and Drug Administration (FDA) assessment of model credibility [9]. However, the high simulation cost of atrial electrophysiology models means that naively propagating uncertainty in model parameters through organ-scale simulations using a Monte Carlo approach is currently intractable. Several works from various engineering fields [10–16] adopted the unscented transform (UT) [17] to tackle the curse of dimensionality, as this sampling technique allows a probability distribution to be presented with a minimal number of samples.

In this paper, we utilise our previously published method [18] to model the shape uncertainty. To allow us to propagate uncertainty in complex simulations, we adopt the unscented transform (UT) to generate samples of the left atrium (LA) anatomy. For each sampled anatomy, we determine the computational model parameters from LGE images following the procedure described in [3], and we simulate the electrophysiology following a cross-field stimulation. The variability in atrial shape also induces variability in surface image intensity ratio (IIR) estimates and thus in tissue material properties. We evaluate the uncertainty arising from both contributions to the produced atrial arrhythmias. Finally, we compare the results with those obtained by adopting a model (i) with uncertainty in the shape only (using the same LGE for each sample shape) and (ii) with uncertainty in the IIR map only (using the same shape for each sample).

We describe the methodology in Section 3 and show the results in Section 4. Section 3.1 summarises the approach that produces the anatomical posterior probability distribution from clinical images. Section 3.2 describes the unscented transform as an effective method for reducing the sample size. Sections 3.3 and 3.4 describe the procedure we follow to generate pre- and post-ablation computational models for each sample. Section 3.5 provides details on the numerical simulations. Section 3.6 describes the algorithm for estimating the characteristic frequency. Section 3.7 details all the possible simulation results and describes the methodology we use to determine the outcome and the distribution. Section 4.1 compares the unscented transform with the Monte Carlo sampling on the image intensity ratio (IIR) and the activation map evaluated with an eikonal model. Section 4.2 compares the simulation result evaluated on the deterministic model with the outcome distribution. Finally, Section 4.3 shows the impact of considering uncertainty in shape or LGE projection only.

2. State of the art

Several groups [3,19–21] have adopted the procedure presented in [4] (or a variation thereof) to quantify atrial fibrosis and thus assign parameter values to a computational model of the left atrium. This approach consists of projecting the LGE intensity onto the atrial surface, evaluating the image intensity ratio (IIR) between the LGE and the mean blood pool, and classifying the tissue as fibrotic when the value of IIR exceeds a given threshold. Assigning to each region model parameters taken from the literature produces a computational model for simulating catheter ablations [19] and evaluating the optimal ablation procedure to inform clinicians [3,20]. All these works do not take into account the uncertainty in the data, hence being prone to discrepancies between the predicted and the obtained outcomes. In our previous paper [18], we quantified the derived uncertainty in the activation map using the Monte Carlo approach with 12,000 samples from the posterior anatomy distribution. We simulated each activation map using an eikonal model with homogeneous material properties [22], and finally, we computed the sample mean and standard deviation. This simplified model, however, captures the sinus rhythm only, not the more complex arrhythmias used in clinical simulations.

3. Method

We generate computer models from ten LGE-MRI images of the LA from a previous study [23] and determine the simulated outcome distribution following the procedure outlined in Fig. 1.

Briefly, we segment LA MRI images (Fig. 1 A; Section 3.1); then, we compute and sample from the posterior probability distribution of the LA anatomy (Fig. 1 B; Section 3.2); next, we project the IIR onto each sampled anatomy and classify the tissue as either normal or fibrotic (Fig. 1 C; Section 3.3). We determine the type of arrhythmia by comparing pre- (Fig. 1 D; Section 3.3) and post-ablation (Figs. 1 E , 1 F; Section 3.4) simulations. Finally, we compute the outcome probability distribution using the simulated samples (Fig. 1 G; Section 3.7)

Shape uncertainty changes the size of an atrium model, and it also causes a change in material properties due to changes in the IIR projection. We test both contributions together and separately. To separate the two effects, we (i) map the projections of the IIR onto the sixteen different shape samples onto the mean posterior anatomy and (ii) assign the sample average of the projected IIR map to each anatomy. We compare the results with those obtained by taking into account both sources of uncertainty. We present the results in Section 4.2

3.1. Left atrium anatomy from image processing

Models are based on anonymised data sets; details of each patient, including gender, age, and atrial fibrillation type, were not available. We segment clinical MRI images (in-plane resolution between 0.92×0.92 and 1.3×1.3 mm; slice thickness of 2 mm) with an open-source platform [24] and generate a shell triangulation from the segmentation to provide a mathematical description of the LA shape. We register the atlas derived from 70 cases in [18] to each triangulated surface, thus obtaining observations $\mathbf{X}_{\mathrm{obs}}$ of the atrial shape with the same topology. For atlas registration, we use Deformetrica [25]. Finally, we estimate the anatomical posterior probability distribution $p(\mathbf{X}|\mathbf{X}_{\mathrm{obs}})$ of the true atrial shape $\mathbf{X}$. We choose the first $N_{\mathrm{modes}} = 15$ principal components to capture ~90% of the cumulative explained anatomical variance [18].

3.2. The unscented transform

We determine the probability distribution of atrial arrhythmias using an empirical distribution. Adopting the default Monte Carlo (MC) approach requires (i) sampling a large number N_{samples} from the posterior $p(\mathbf{X}|\mathbf{X}_{\mathrm{obs}})$; (ii) solving the computational model with each sample; and then (iii) looking at the sample distribution. The computational
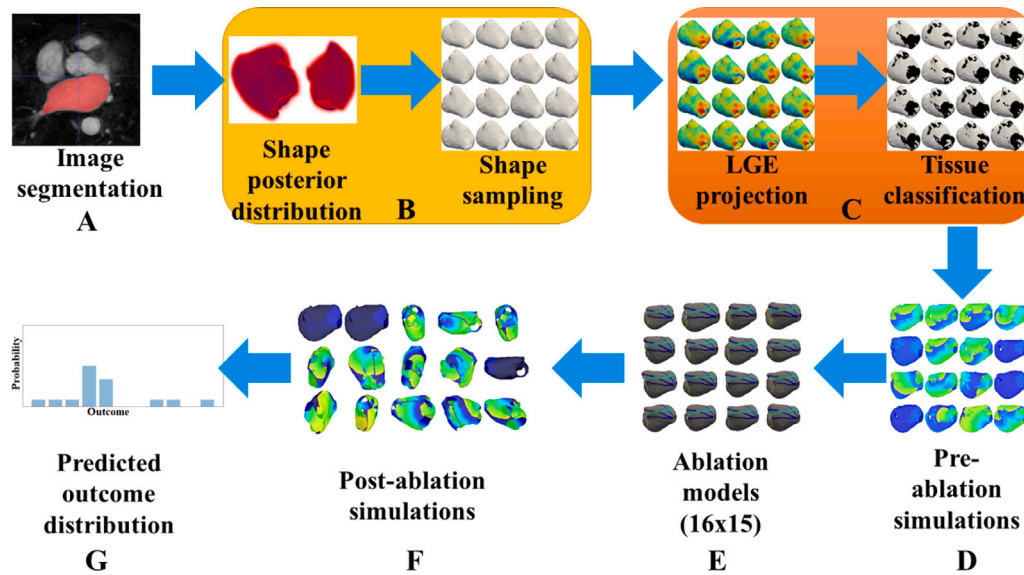
Fig. 1. Outline of the procedure we follow to compute the probability distribution of arrhythmias, for each clinical case. We segment MRI images (A). We compute the posterior distribution of LA shape samples (B). We project the image intensity ratio onto each sample and classify the tissue as normal or fibrotic (C); we also generate 15 models of ablations (E). We simulate pre- (D) and post-ablation (F) electrophysiology to classify the arrhythmias into 34 possible outcomes and compute their probability distribution (G).

cost associated with electrophysiological simulations makes it impossible to adopt this approach. To overcome these difficulties, we adopt the unscented transform (UT) [16,17], consisting of computing n σ-points from $p(\mathbf{X}|\mathbf{X}_{\text{obs}})$ and then propagating these through the simulator. For linear Gaussian problems, UT is exact with $N_{\text{modes}} + 1 = 16$ σ-points.

We validate the accuracy of the UT representation of the posterior LA distribution against MC sampling in two ways: (1) quantifying the uncertainty in atrial fibrosis burden due to anatomy uncertainty and (2) quantifying the uncertainty in local activation times, calculated using an eikonal model, due to uncertain anatomy. Using ten clinical cases, we compare the fibrosis and activation map statistics (mean and standard deviation) of $N_{\text{samples}} = 16$ UT samples against $N_{\text{samples}} = 12{,}000$ random Monte Carlo samples. We provide details and results in Section 4.1.

3.3. Pre-ablation computational models

Projection of the LGE image intensity onto the surface mesh provides an estimate of the fibrosis map and thus can be used to inform heterogeneous tissue properties when simulating atrial electrophysiology [3,26].

For each clinical case, we project the LGE image intensity onto each anatomical sample. Next, we compute the image intensity ratio (IIR) between the local LGE intensity and the mean blood pool (mBP) and classify as fibrotic the portions of tissue with IIR ≥ 1.22 [3,4].

We describe the human atrial action potential using the Courtemanche (CRN) model [27], and we characterise the myocardial tissue as a monodomain isotropic medium. Table 1 summarises the parameter values we use in numerical simulations.

For the non-fibrotic myocardium, we assign the default parameter values of the CRN model [27] and a conductivity $\Sigma_{\text{mono}} = 0.1289$ S/m, which provides a conduction velocity of 43.39 cm/s [3,26], consistent with conduction velocities measured in AF patients [28]. We characterise the fibrotic tissue with a 40% down-regulation of G_{Na}, a 50% down-regulation of G_{K1} and G_{CaL} [3,26], and a conductivity reduced by 40%. This represents a remodelling yielding a +15.4% APD, a −7.18% resting trans-membrane voltage v_{m}, and a −49.6% upstroke velocity, consistent with those documented in fibrotic atrial myocardium in vitro [29] and a decreased intracellular coupling produced by collagen deposition and gap junction remodelling [30,31]. Finally, we refine each computational mesh to a spatial resolution of 300 μm.

Table 1
Parameter values characterising the myocardial tissue. We assign the default parameter values of the CRN model to the non-fibrotic myocardium with a conductivity Σ_{mono} of 0.1289 S/m. This value yields a conduction velocity equal to 43.39 cm/s, within the range of values recorded in patients with AF. For the fibrotic myocardium, we assign the ionic parameters that characterise a fibrotic remodelling, yielding a +15.4% APD, a −7.18% resting trans-membrane voltage [Vm], a −49.6% upstroke velocity, and a reduction in conductivity of 40%.

	Σ_{mono} (S/m)	G_{Na} (nS/pF)	G_{K1} (nS/pF)	G_{CaL} (nS/pF)
Non-fibrotic	0.1289	7.8	0.09	0.1238
Fibrotic	0.05503	−40%	−50%	−50%

3.4. Post-ablation computational models

In each of the ten atrial anatomical models considered here, there are a total of six holes in the atrial shell: four pulmonary veins, a left atrial appendage, and a mitral valve. Hence, there are fifteen unique ablation lines to consider if we wish to terminate a macro-re-entry around an anatomical structure by ablating along lines that connect a pair of holes (Fig. 2, left). Thus, each anatomical sample produces $N_{\text{abla}} = 15$ post-ablation model simulations.

We obtain each post-ablation model by adding an ablation line (Fig. 1 E) with a width of 1 mm. Each line represents the shortest geodesic path between a pair of geometrical singularities (holes). We assign the ionic parameters of the fibrotic tissue and a negligible conductivity ($\Sigma_{\text{mono}} = 0.5 \times 10^{-3}$ S/m) to the ablated tissue.

3.5. Numerical simulations

We simulate pre- (Fig. 1 D) and post-ablation arrhythmia (Fig. 1 F) using the Carpentry simulator (available at https://carp.medunigraz.at) with a time step of 5 μs and no mass lumping. We ran simulations on Archer2 (https://www.archer2.ac.uk), the national HPC facility, using array jobs (max running jobs:16; max queued jobs:64) with 128 cores per simulation. A wall time of 24 h was enough to complete both pre- and post-ablation simulations.

Pre-ablation. We initialise the cellular electrophysiology model to the limit-cycle values calculated by running the 0D simulated cell model for 500 stimuli at a basic cycle length (BCL) of 300 ms. We initiate the arrhythmia using a cross-field stimulation in the regions
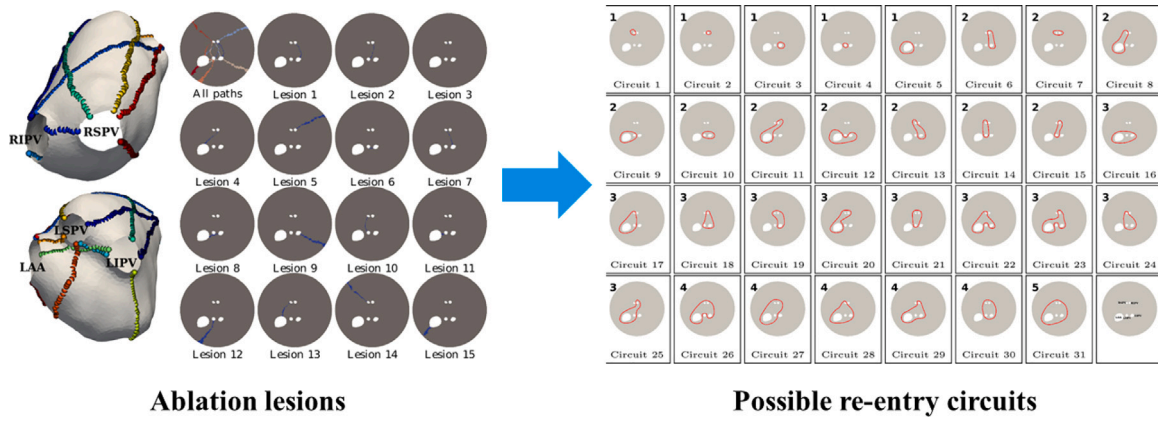
Fig. 2. Left: Ablation lesions we use to identify the re-entry circuits. Right: Re-entry circuits that are affected by the N_{abla} ablations. We represent the left atrium with the unfolding proposed in [32].
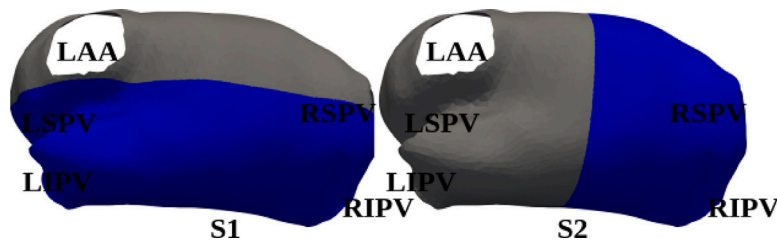

Fig. 3. We initialise the cell model to the limit cycle, running 0D simulations of 500 stimuli at a BCL of 300 ms. We initiate the arrhythmia with a cross-field protocol. We apply the S1 stimulus at the lateral-inferior-septal regions. We then stimulate at time S2 in the following regions: septal; right antral; and right half of inferior, anterior, and posterior.

shown in Fig. 3, calibrated to induce an arrhythmia for each patient with S2 between 240 and 260 ms.

We simulate 35 s of electrical activity to reach a stable AT or AF activation (or a termination). For the last five simulated seconds, we compute the characteristic frequency (CF, Section 3.6) and the time-averaged phase singularity (PS) map [33,34].

We save the solutions at three checkpoints 100 ms apart (T1 = 30100, T2 = 30200, T3 = 30300) to use them as the initial condition in post-ablation simulations. This is to ensure that the time the ablation is applied does not impact the classification.

Post-ablation. We compute post-ablation simulations with a duration of 5 s, initiated at the checkpoints saved from the pre-ablation simulations. For the simulation from each checkpoint, we evaluate the dominant frequency (DF) map using the tools implemented in CARPentry[1] and its spatial median. Finally, we choose the case presenting the highest median DF as the post-ablation simulation.

3.6. Computing the characteristic frequency of atrial tachycardia

Denoting by v_m the trans-membrane potential, we define the characteristic frequency (CF) as the inverse of the characteristic time T, such that $v_m(t + T, x) = v_m(t, x)$, for all t. We evaluate CF from N_t temporal samples $\Delta t = 5$ ms apart of the v_m traces, simulated on a mesh of N_p points. We proceeded as follows.

Denoting by $v_m^{k,j} = v_m(t_k, x_j)$ the numerical solution at time t_k and location x_j and by $v_m^{ref,j}$ the same solution at k=N_t/2, we compute

$$y(t_k) = \frac{1}{N_p} \sum_{j=1}^{N_p} |v_m^{k,j} - v_m^{ref,j}| \tag{1}$$

and then we shift y by its mean and re-scale the result by its standard deviation: $\hat{y} = (y - \bar{y})/\sigma_y$. Finally, we compute the Fourier transform of $\hat{y}$ and define CF as the frequency with the largest spectrum.

---

[1] Documentation available at the following URL: https://carpentry.medunigraz.at/getting-started/.

3.7. Numerical simulation outcomes and outcome distribution

There are a total of 31 distinct pathways (Fig. 2, right), involving the four pulmonary veins and the appendage (anatomical structures): five around one structure, ten around two structures, ten around three structures, five around four structures, and one around five structures (see Table A.3 in Appendix A for the mapping between the index number assigned to each circuit and the structures it goes around). We will refer to these pathways as macro-re-entries.

To take into account arrhythmias that depend on the tissue substrate, we introduce an outcome in which a static rotor goes around tissue heterogeneity but not around any anatomical structure (in what follows, we will refer to this pathway as functional re-entry). We classify all other re-entrant activation patterns, including a meandering rotor, as AF. Thus, there are a total of 34 outcomes:

- 31 macro-re-entries
- a static rotor around tissue heterogeneity
- atrial fibrillation
- arrhythmia that terminates within 30 s.

During AF, we expect a chaotic activation pattern with PS appearing across the atria and not predominantly located in a local region. We quantify this by measuring the spatial median of the PS density, assuming that this value will be above zero in AF. This means that if a PS occurs over 50% of the atrial surface in a 5-second period, we classify this activation pattern as AF.

We assume that if the driving activation path that determines the dominant frequency of AT passes around an anatomical structure (hole), then ablating a line between this structure and any other structure will cause a change in the activation wave path and hence a change in the characteristic frequency (CF) introduced in Section 3.6. By calculating the change in CF (ΔCF) following ablation, we can test whether an ablation line cuts the critical activation path, allowing us to identify between which anatomical structures the dominant activation wave passes . We use a threshold of 10% change in CF as a clinically
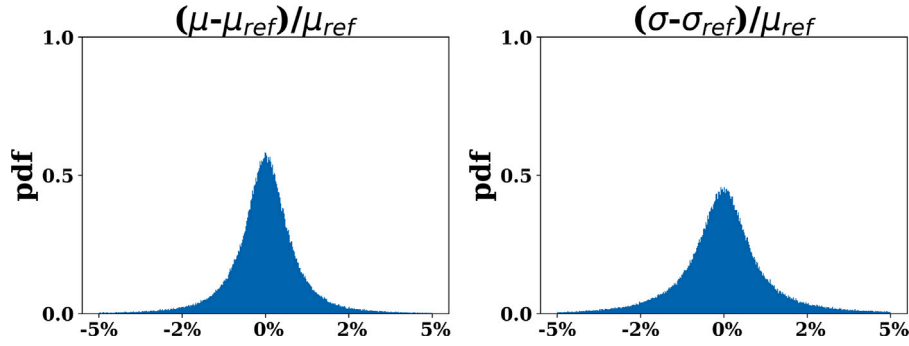
Fig. 4. Relative point-wise discrepancies between UT and MC sampling in the sample mean IIR map (left) and sample standard deviation IIR map (right). We assume MC to be the ground truth.

meaningful change, as proposed by [35]. However, it is possible that smaller changes in CF indicate a change in path. To account for this possibility, we introduce an ablation label S_{abl} (Eq. (2)), which has a value of 0 for no change in CF, a value of 1 for a 10% change, and a value in the range [0, 1] for a change in CF between 0% and 10%:

$$S_{abl} = \begin{cases} 0 & \Delta CF/CF_{pre} \leq 0 \\ (\Delta CF/CF_{pre})/0.1 & 0 < \Delta CF \leq 0.1 \\ 1 & \Delta CF/CF_{pre} > 0.1 \end{cases} \quad (2)$$

To define a circuit, we first define the mapping $\mathcal{M}_{C \rightarrow A}$ between each circuit C_i (Fig. 2, right) and the set of ablation lines $\mathcal{A}_j$ (Fig. 2, left) that cut C_i.

A stable functional re-entry around a tissue heterogeneity does not present any circuits: thus (ideally) none of the ablations will interfere with the activation; however, if an ablation crosses the region anchoring the rotor, it may still cause a change in CF.

For the 31 macro-re-entries and for a re-entry around a tissue heterogeneity, we define the scores of Eq. (3) that depend on the ablation effectiveness defined in Eq. (2). as follows:

$$S_{circuit} = \begin{cases} \left(\sum_{k=1}^{N_{C_i}} S_{abl}^{\mathcal{M}_{C \rightarrow A}^k(C_i)} \right)/N_{C_i} & C_i = 1 \dots 31 \\ \left(\sum_{k=1}^{N_{abla}} \left(1 - S_{abl}^k \right) \right)/N_{abla} & C_i = 32 \end{cases} \quad (3)$$

Scores fall within the range [0, 1]. We point out that these scores do not represent probabilities. We denote by N_{C_i} the number of ablation lines affecting C_i and by $\mathcal{M}_{C \rightarrow A}^k(C_i)$ the kth element of the set of ablation indices affecting the circuit C_i.

For example, if all ablation lines that include the left atrial appendage cause a change in CF, then we conclude that the activation pattern must go around the left atrial appendage. A functional re-entry presents an empty set.

For simulations leading to AF, we assign $S_{circuit} = 1$ to $C_i = 33$ and $S_{circuit} = 0$ to the others. For simulations that do not present a sustained arrhythmia, we assign $S_{circuit} = 1$ to $C_i = 34$ and $S_{circuit} = 0$ to the others.

We assign the circuit C_i with the largest $S_{circuit}$ to each sample. Finally, we compute the probability of each C_i as the number of its recurrences within the $N_{samples}$ samples divided by the total number of samples, $N_{samples}$. For example, if circuit C_i recurred N_{C_i} times, we assign the probability $N_{C_i}/N_{samples}$. This provides an estimate of the probability of a given arrhythmia being present given the uncertainty in the anatomy (Fig. 1 G).

4. Results

Simulated arrhythmias present the following characteristic frequencies (mean ± std): macro-re-entries (2.82 ± 0.4 Hz), functional re-entries (2.81 ± 0.48 Hz), and atrial fibrillation (3.02 ± 0.25 Hz). These values are marginally slower but fall within the reported range of atrial arrhythmias [36].

4.1. Validation of the unscented transform

We validate the unscented transform, comparing it against the Monte Carlo estimates of IIR and the activation patterns.

For each clinical case, we draw $N_{samples} = 12{,}000$ i.i.d. samples from the posterior LA distribution $p(\mathbf{X}|\mathbf{X}_{obs})$. For each sample, we follow the procedure described in Section 3.3 to generate 12,000 pre-ablation models. First, we project the LGE score onto the mesh. Second, we compute IIR and identify fibrosis. Finally, we generate a computational model that uses the fibrosis label to introduce tissue heterogeneity. To test whether the UT can be used to estimate uncertainty in image-based operations, we compare UT and MC estimates of uncertainty in IIR.

We then test whether UT can be used for simulations. We compare UT and MC estimates of uncertainty in simulations that predict activation times computed with the eikonal model described in [22]. For the eikonal model, we use the CV produced by the modified Mitchell and Schaeffer model (mMS) [37], with $\tau_{in} = 0.1$ ms, $v_{gate} = 0.1$, and the conductivity values introduced in Table 1.

In both tests, we compute the distribution of the discrepancy between the maps of the sample mean and the sample standard deviation obtained with UT and MC.

For a given map $U(x, y, z)$, we compute the sample mean and the sample standard deviation maps as follows:

$$\mathbb{E}[U(x, y, z)] \approx \frac{1}{N_{samples}} \sum_{k=1}^{N_{samples}} U^k(x, y, z) \quad (4)$$

$$\mathbb{V}ar[U(x, y, z)] \approx \frac{1}{N_{samples} - 1} \sum_{k=1}^{N_{samples}} (U^k(x, y, z) - \mathbb{E}[U(x, y, z)])^2 \quad (5)$$

Here we consider the maps obtained from 12,000 samples as the ground truth.

IIR. We compute the discrepancies between the UT and MC sampling techniques in the sample mean and the sample standard deviation of the distribution of fibrosis across the atria. We express the discrepancies as the percentage w.r.t. the reference mean. Fig. 4 shows the overall distribution.

In Appendix B, we present the mean IIR map, the map of the IIR standard deviation, and the probability map of the fibrosis computed with 12,000 i.i.d Monte Carlo samples and with the unscented transform.

Local activation times. Fig. 5 shows the overall distribution of the discrepancies in LAT maps, evaluated with the two sampling techniques.

In Appendix B, we present the mean LAT map and the map of the LAT standard deviation, computed with 12,000 i.i.d Monte Carlo samples and with the unscented transform. To test whether 12,000 samples are sufficient, in Appendix C we show that with $N_{samples} \geq 7000$ the mean std varied by <1%.
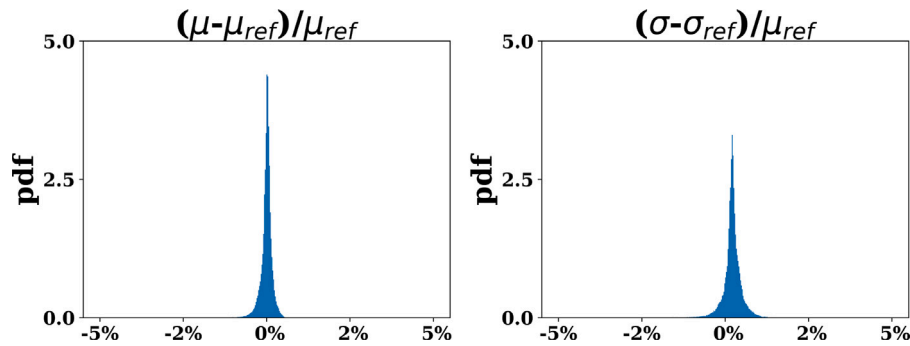
Fig. 5. Relative point-wise discrepancies between UT and MC sampling in the sample mean activation map (left) and sample standard deviation activation map (right). We assume MC to be the ground truth.

Table 2

Comparison of the outcome of the deterministic model with the outcomes of the statistical model. "Deterministic model outcome" denotes the outcome of the deterministic methods. "In statistical" indicates whether the statistical model also produced the outcome of the deterministic model. "Probability" indicates with which percentage the statistical model produces the same outcome as the deterministic model. "Rank" denotes the ranking of the deterministic outcome (first if it has the highest number of recurrences, second if it has the second-highest numbers of recurrences, and so on). When other outcomes have the same rank, the total number with the same rank is reported in brackets. LIPV: left inferior pulmonary vein; LSPV: left superior pulmonary vein; RIPV: right inferior pulmonary vein; RSPV: right superior pulmonary vein.

Case	Deterministic model outcome	In statistical	Probability (%)	Rank
1	LIPV re-entry (3)	yes	12.5	3 (3)
2	RIPV re-entry (2)	no	0	N/A
3	RSPV re-entry (1)	yes	12.5	4
4	RSPV re-entry (1)	yes	12.5	3 (2)
5	Functional re-entry(32)	yes	6.25	3 (6)
6	LIPV re-entry (3)	yes	6.25	4 (4)
7	Atrial fibrillation(33)	yes	50	1
8	RIPV re-entry (2)	yes	12.5	5
9	Functional re-entry(32)	yes	56.25	1
10	No arrhythmia (34)	yes	12.5	3 (3)

4.2. Uncertainty in the type of arrhythmia

For each clinical case, we also generate pre- and post-ablation computational models directly from the image segmentation, not accounting for shape uncertainty (we will refer to this model as deterministic); we simulate atrial arrhythmia as described in Section 3.5, evaluate the characteristic frequency (Section 3.7) and finally determine the AT circuit (Section 3.7).

We compare the outcome of each deterministic model with the outcome distribution obtained from the statistical model. We check whether distribution of the statistical model also contains the outcome obtained with the deterministic model, its probability, rank, and number of rank pairs.

Table 2 summarises the results, and Fig. 6 plots the statistical distribution of the simulation results for each clinical case (red bars). The same figure also plots the statistical distribution when taking into account the uncertainty in the LGE projection only (blue) and the shape only (green).

Some cases are clearly more prone to substrate arrhythmia (Cases 2,7, and 9) or macro-re-entry (Cases 1, 3, 5, 6, 8, and 10), while others present a mix across both (Case 4). Consistent with the images obtained from AF patients, we see that self-termination was never the most common activation pattern.

Except for Case 2, the statistical model contains the outcome of the deterministic model.

In Case 2, in the deterministic model, we identified a right inferior pulmonary vein (RIPV) re-entry AT as the driver; on visual inspection, we found that the RIPV re-entry was the driver, but it also entrained a functional re-entry. This functional re-entry was the most likely outcome of the statistical models (37.5%), and the RIPV circuit was not present.

In Cases 7 and 9, the outcome of the deterministic model coincides with the first-ranked outcome of the statistical model. In both cases, the first-ranked outcome has a probability of at least 50%.

In all other cases, the statistical model predicts that the deterministic outcome was a plausible outcome, with a probability ranging from 6.25% to 12.5%, but not the most likely outcome.

4.3. Shape uncertainty and LGE projection uncertainty

We then separate the effects of uncertainty in shape on anatomy and material properties. To isolate the impact of uncertainty in LGE alone, we use the posterior mean as the atrial anatomy for all the samples; we then fix the LGE to the sample mean to focus on uncertainty in shape only.

Fig. 7 summarises the outcomes for all the ten cases and all the sixteen samples when the anatomy only (USHAPE, green), the LGE projection only (ULGE, blue), or both (UBOTH, red) produce uncertainty.

USHAPE presents simulations with fewer AF or functional re-entries ($\simeq$18%), when compared with UBOTH ($\simeq$33%) and ULGE($\simeq$35%). The occurrences of the self-terminating arrhythmias are comparable between UBOTH and USHAPE ($\simeq$14%) and twice frequent as with ULGE ($\simeq$7%), while there is an increase in macro-re-entries (outcomes 1–31; $\simeq$68%) compared with UBOTH ($\simeq$54%) and ULGE ($\simeq$58%).

Functional re-entries are comparable between UBOTH ($\simeq$23%) and ULGE ($\simeq$24%)simulations and occur more than in USHAPE ($\simeq$14% simulations). This is replicated by AF (UBOTH: $\simeq$9%; ULGE: $\simeq$11%; USHAPE: $\simeq$4%).

Neglecting the uncertainty in the LGE projection leads to an overestimation of the macro-re-entries and an underestimation of the functional re-entries, while non-sustaining arrhythmias are unaffected.

Neglecting the uncertainty in shape leads to an underestimation of cases of non-sustaining arrhythmias.

5. Discussion

In this study, we have shown how the unscented transform (UT) can be used to propagate uncertainty in anatomy through electrophysiology simulations to provide predictions of AF ablation outcomes with uncertainty. We have proposed a general framework for describing and classifying AT/AF. We have shown that deterministic simulations do not necessarily provide predictions of the most likely outcome. Finally, we demonstrated that uncertainty in anatomy was more important for determining macro-re-entries and terminations, while uncertainty in LGE was more important for functional re-entries.

Unscented transform. Clinical measurements are often subject to noise and artefacts. This gives rise to uncertainty in anatomical structures, which in turn can lead to uncertainty in model predictions. Sampling shape uncertainty with Monte Carlo samples will require a large
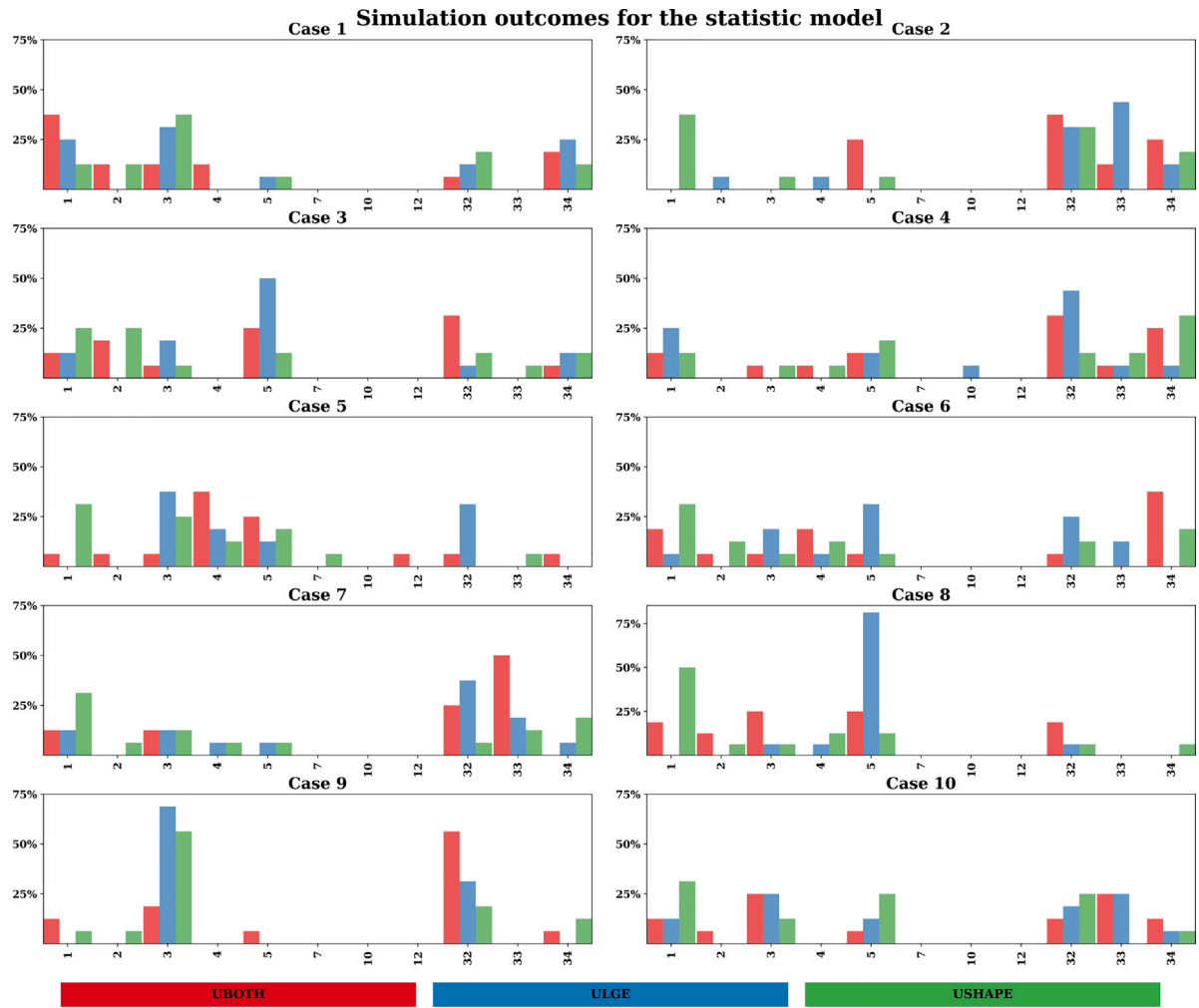
Fig. 6. Outcome frequencies in each case, when uncertainty affects the shape and LGE projection (red), the LGE projection only (blue), and the shape only (green). For clarity, we removed the outcomes that never occurred. The labels represent the circuits in Fig. 2 and Table A.3.
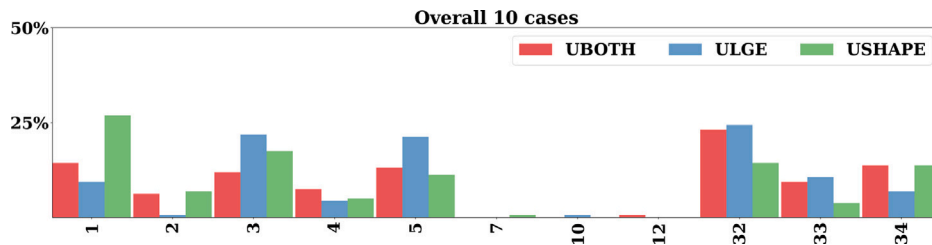

Fig. 7. Recurrences when shape and LGE projection are uncertain (red), when LGE projection only is uncertain (blue), and when shape only is uncertain (green). For clarity, we removed the outcomes that never occurred.

number of samples ($>10,000$). Each sample is expensive to create and requires multiple expensive simulations. This makes MC not tractable for propagating anatomical uncertainty through complex multi-scale simulations of procedure outcomes. The unscented transform [17] requires $d + 1$ samples to represent the uncertainty in d parameters, and it is second-order accurate when the distribution is Gaussian. The UT effectiveness in evaluating the uncertainty of non-linear models in indirect measurements has been demonstrated [17]. The UT represents a powerful tool in statistical applications, such as learning a simplified representation of a Gaussian mixture model [15], non-linear Kalman filtering [16], and its applications in engineering fields (electrophysiology: [14]; monitoring of power system dynamics: [13];

aerospace: [10,12]; fault diagnosis: [11]). Consistent with these successful applications, we have verified the benefits of UT for propagating shape uncertainty in LGE measurements and electrophysiology simulations of the atrium.

Uncertainty in the type of arrhythmia. Left atrial shape is an independent predictor of AF recurrences after ablation that improves patient stratification when combined with fibrosis [38]. Here we show that uncertainty in shape derived from CMR segmentation leads to multiple different predicted arrhythmias, with few cases having a single dominant predicted arrhythmia. Further, the deterministic model does not necessarily represent the most likely outcome in all cases. This highlights the need for improved imaging, either through improved CMR protocols [39] or through the use of more accurate modalities, for example, CT for creating predictive models of AF ablation therapy.

Variations in the atrial shape caused a change in the simulated arrhythmia patterns in all ten patients considered in this study (Fig. 6). In eight out of ten cases, variation in shape led to the termination of the arrhythmia, demonstrating the potential impact of anatomy uncertainty on atrial arrhythmia predictions. We classified the arrhythmias by introducing topologically defined lines of block or ablations; these topological lines were not impacted by shape variability. When a line crosses the path of the pre-ablation atrial tachycardia, it reduces the characteristic frequency, indicating the critical path of the re-entry. When, conversely, anatomical samples generate functional AT or AF, the introduction of lines of block for different shape samples caused different outcomes. This demonstrates that shape can potentially affect both the pre-ablation arrhythmia and the simulated impact of ablations on atrial fibrillation. Although in this study we did not simulate therapeutic ablations targeted to a specific arrhythmia, it is possible to extend the approach to simulate the effect of uncertain shape on pulmonary vein isolation, substrate medication, or pharmacologic therapies.

Comparison with previous works. Previous groups have simulated patient atrial arrhythmia (for a review, see [40]). Many of these studies have focused on simulating atrial fibrillation. A limited number of groups have focused on simulating atrial tachycardia and predicting the type of re-entrant activation [20,41,42]. However, these studies have not dealt with the quantification of uncertainty in predictions of re-entrant activation type or the effect of uncertainty in shape on simulations. Previous studies by us [43] and others [44–46] have developed methods for quantifying uncertainty in activation maps, used to calibrate atrial models and to capture uncertainty in material properties. However, all these approaches assume deterministic anatomy, thus not accounting for uncertainty in shape. The study by [47] investigated the sensitivity of simulations of the cardiac function of the whole heart to the shape. They created an emulator that mapped statistical shape models onto simulated functional outputs. However, none of these studies have performed sampling over the shape space to propagate uncertainty in shape forward into simulation predictions. Monte Carlo sampling is presently not computationally tractable with patient-specific fibrillation simulations. Polynomial chaos methods such as the one presented in [48] are intrusive and so may require code rewrites. While this could be an option in some applications, there are many cases in which it is not possible or desirable to amend the code. In this paper, we used the unscented transform as a low-cost non-intrusive method for propagating uncertainty in our model. We classified the type of activation by looking for meaningful changes in activation times following ablations between distinct topological structures in the atrial mesh. Alternative approaches for classifying atrial tachycardia include directed graph mapping [42]; however, most of these approaches require parameter tuning. Moreover, these methods do not differentiate the principal driver from the bystanders and do not identify atrial fibrillation, so they can fail to correctly classify an arrhythmia. Approaches based on flutter loops [41] are computationally convenient; these methods, however, identify neither functional re-entries nor atrial fibrillation, thus making them unsuitable for this study. We have provided a tractable approach for accounting for shape uncertainty in atrial simulations and characterising atrial arrhythmia.

Research gaps. Adopting cardiac models to predict outcomes [2,3,19] poses three challenges. First, models are generated from images that can be acquired only once and are recorded from sick patients that may have implants. It is not possible to guarantee that all images will be of diagnostic quality. Nevertheless, all patients will receive treatment, and a simulation guidance platform should be as robust as possible to the input data while estimating confidence in the predictions based on the quality of the input data. The adoption of methods that account for uncertainty will give the best estimate of the outcome and the best estimates of simulation confidence with the data available. Second, current workflows for the creation of patient-specific atrial models have several manual steps, making the process time-consuming.

However, our approach allows operators to perform quality control checks during model development. Estimating the effect of image quality on model predictions provides an automated data quality check that would facilitate the adoption of automated methods. Third, our current model creation workflow generates personalised atrial models from a combination of two CMR scans: an MRA scan to measure anatomy and an LGE scan to measure fibrosis. Taking two scans requires more time but allows a more accurate shape estimate from the MRA scan than is achievable with the LGE scan. The effects of shape uncertainty on model predictions are not known, and it would be useful to understand how shape uncertainty impacts simulation predictions. This study combines an existing method for quantifying shape uncertainty from medical images with a tractable method for propagating shape uncertainty through to patient-specific simulation predictions, creating a new approach that allows estimating the impact of image quality on simulation predictions.

Areas that may need to be improved to reduce image uncertainty. The time between LGE administration and image acquisition [49], and the large inter-individual breath-hold-to-breathing variations [50] are all factors that introduce uncertainty in LGE imaging. Quantifying how this affects the numerical simulations has the potential of improving personalised ablation strategies.

Shape uncertainty and LGE projection uncertainty. Models with only uncertainty in the anatomy produced more maco-re-entries than models with both uncertainty contributions and the same number of self-terminating arrhythmias. Models with only uncertainty in LGE had recurrences of functional re-entry and atrial fibrillation comparable to those in models characterised by both contributions. These results are consistent with [51,52], who ascribed macro-re-entries to atrial dimensions that are large enough to sustain a re-entry circuit, and with [53], who correlated the two pathological conditions with the fibrotic substrate of the tissue.

6. Limitations

Classification of the arrhythmia. We classified arrhythmias by a meaningful change between pre- and post-ablation characteristic frequencies. When two re-entrant circuits coexist with very similar CF, a single ablation line does not cause a change in CF, thus yielding a misclassification. Simulating combinations of ablations would reduce this but would increase the number of required simulations. Alternatively, we found that only a subset of macro-re-entry AT was present, so a refined experimental design of the ablations could reduce the computation. The current approach does not detect secondary drivers; this caused the statistical model to not identify the deterministic activation pattern. Alternative approaches look at activation loops and can detect potentially secondary activation patterns [41,42]; however, the resolution of these approaches is unable to differentiate between macro-re-entries and functional re-entries in close proximity to anatomical structures.

Initiation of the arrhythmias. We used a simple simulation protocol to test for an arrhythmia. Other groups have proposed different pacing protocols [20] to explore more in depth the sustainable arrhythmias in a given atrial model. We used a lower-cost initiation protocol for the arrhythmia to demonstrate the uncertainty propagation method; more complex pacing protocols would be equally applicable but would further increase the computational cost. We used a FEM simulator on a conventional CPU for these simulations, with each stimulation taking 24 h on 128 cores. The development of GPU simulators [54] may drastically reduce the cost of simulations. Adopting these new simulators may be essential for enabling computationally tractable anatomical UQ.

Sampling. To consider N central moments, the unscented transform requires $N \times (N_{modes} + 1)$ samples [17], making the problem computationally intractable. The shape distribution, however, is Gaussian, making $(N_{modes} + 1)$ samples ($N = 1$) adequate to capture shape uncertainty. Numerical tests demonstrated an error that is comparable to the error in measurements.

Table A.3
Mapping between circuit and structures.

1 structure		2 structures		3 structures	
1	RSPV	6	(RIPV, LIPV)	16	(LSPV, LIPV, LAA)
2	RIPV	7	(RIPV, RSPV)	17	(LSPV, RSPV, LAA)
3	LIPV	8	(RSPV, LAA)	18	(LSPV, LIPV, RIPV)
4	LSPV	9	(LSPV, LAA)	19	(LIPV, RSPV, RIPV)
5	LAA	10	(LSPV, LIPV)	20	(RSPV, RIPV, LAA)
		11	(RIPV, LAA)	21	(RSPV, RIPV, LSPV)
		12	(LAA, LIPV)	22	(RSPV, LIPV, LAA)
		13	(RSPV, LIPV)	23	(RIPV, LIPV, LAA)
		14	(RSPV, LSPV)	24	(RSPV, LSPV, LIPV)
		15	(RIPV, LSPV)	25	(LSPV, RIPV, LAA)

4 structures		5 structures	
26	(LAA, LIPV, RSPV, RIPV)	31	(LSPV, LIPV, RSPV, RIPV, LAA)
27	(LAA, LSPV, RSPV, RIPV)		
28	(LAA, LSPV, LIPV, RSPV)		
29	(LAA, LSPV, LIPV, RIPV)		
30	(LSPV, LIPV, RSPV, RIPV)		

7. Future studies

In this study, we propagated the uncertainty in shape to the identification of tissue properties and, finally, the type of simulated arrhythmia. We explored the possible arrhythmias a patient's atrium can sustain when uncertainty affects the clinical data. We did not explicitly consider the impact of shape uncertainty on predicting the therapy outcome.

Future studies could consider how shape and structure uncertainty impact therapies, including substrate ablation, pulmonary vein isolation, or pharmacological rhythm control. Future studies could consider predicting arrhythmia type and path from pre-procedure imaging data for patients indicated for an ablation procedure to provide further validation of both model predictions and the degree of uncertainty.

8. Conclusions

We have developed, tested, and demonstrated a method for propagating shape uncertainty in atrial models through to uncertainty in predictions of procedure outcomes and demonstrated that uncertainty in shape and fibrosis is more important for predicting macro-re-entry and functional re-entry.

Declaration of competing interest

The authors declare that they have no known competing financial interests or personal relationships that could have appeared to influence the work reported in this paper.

Acknowledgements

Appendix A. Mapping between circuits and structures

Table A.3 shows the map between each circuit and the corresponding structures.

Appendix B. Discrepancies between UT and Monte Carlo sampling

Fibrosis. Fig. B.8 shows the maps of the mean IIR, computed with 12,000 Monte Carlo samples (top row) and with the unscented transform (bottom row); Fig. B.9 shows the maps of the standard deviation.

Fig. B.10 shows the fibrosis probability obtained with 12,000 Monte Carlo samples (top row) and with UT sampling (bottom row). Pointwise, we computed the fibrosis probability as the number of samples presenting fibrosis in a specific location, divided by the total number of samples.

Local activation times. Fig. B.11 shows the maps of the mean LAT, computed with 12,000 Monte Carlo samples (top row) and with the unscented transform (bottom row); Fig. B.12 shows the maps of the standard deviation. We evaluated LAT using the eikonal model presented in [22], with $\tau_{\mathrm{in}} = 0.1\,\mathrm{ms}$, $v_{\mathrm{gate}} = 0.1$, and the conductivity values introduced in Table 1.

Appendix C. Convergence of the number of samples

Fig. C.13 shows the spatial average of the sample mean LAT map (left) and of the sample standard deviation LAT map as a function of the number of samples. A number of samples $N_{\mathrm{samples}} \geq 7000$ allows a variation $<1\%$ for the mean and the standard deviation.

Appendix D. Type of outcome

Fig. D.14 shows the percentage of samples that sustain a macro-re-entry or a substrate-driven re-entry (functional AT and AF) and that do not sustain arrhythmias, when the anatomy only (USHAPE, green), the LGE projection only (ULGE, blue), or both (UBOTH, red) produce uncertainty.

Table D.4 reports the percentage of the sampled anatomies that sustained re-entry for each case, when the anatomy only (USHAPE), the LGE projection only (ULGE), or both (UBOTH) produce uncertainty.

Appendix E. Construction of the shape probability model

We used our semi-automatic workflow [24] to segment atrial MRI images (in-plane resolution of 0.94 mm and slice thickness of 2 mm), crop the left atrial appendage and pulmonary veins at the ostium, and remove the mitral valve from the shell and generate a triangulation of the 2D manifold. We next used the diffeomorphism method implemented in Deformetrica [25] on a mesh surface with $N_{\mathrm{pt}} = 13{,}569$ points to generate an atlas and to register the atlas to each patient's atria, thus obtaining anatomies with a correspondence between mesh points. We represent each anatomy with the following vector: $\mathbf{X} =$
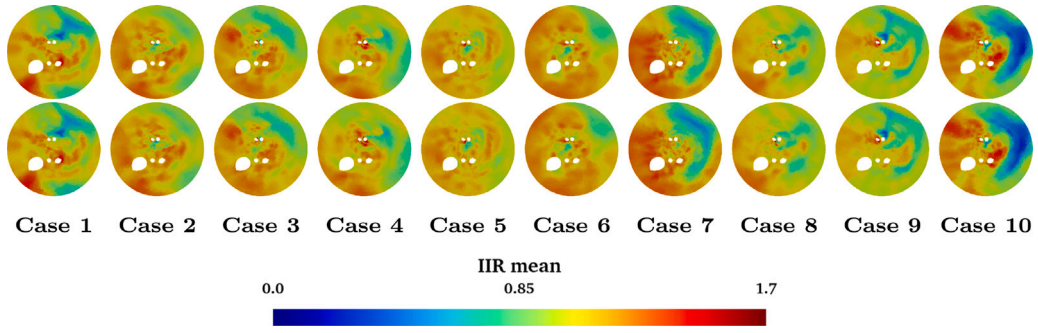
Fig. B.8. Maps of the mean IIR, computed with 12,000 MC samples (top row) and with the unscented transform (bottom row).
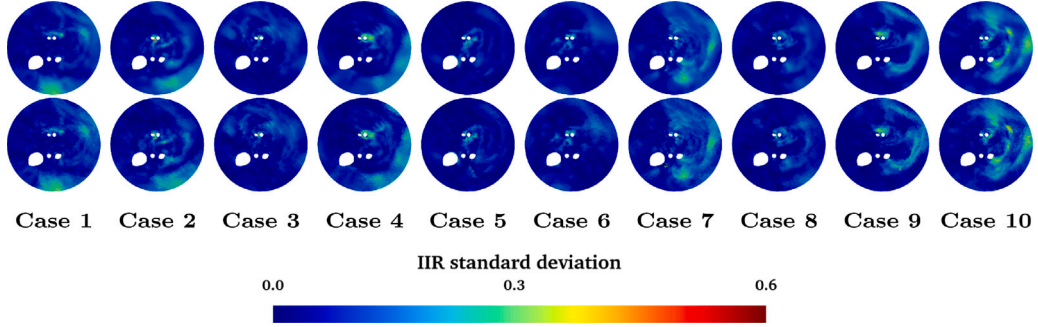

Fig. B.9. Maps of the IIR standard deviation, computed with 12,000 MC samples (top row) and with the unscented transform (bottom row).
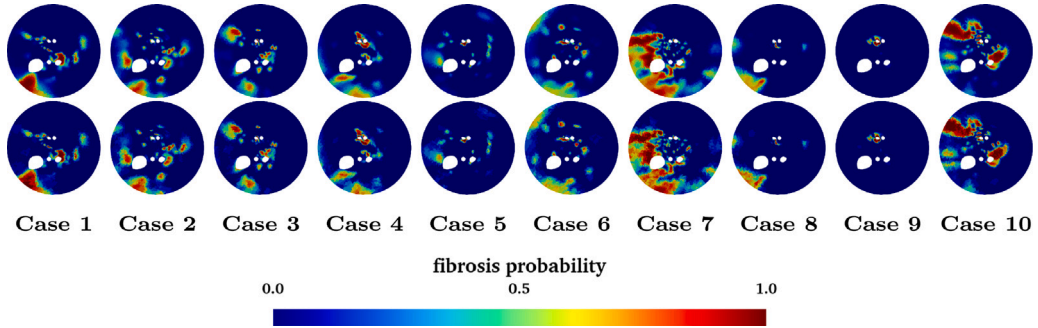

Fig. B.10. Maps of the fibrosis probability, computed with 12,000 MC samples (top row) and with the unscented transform (bottom row).
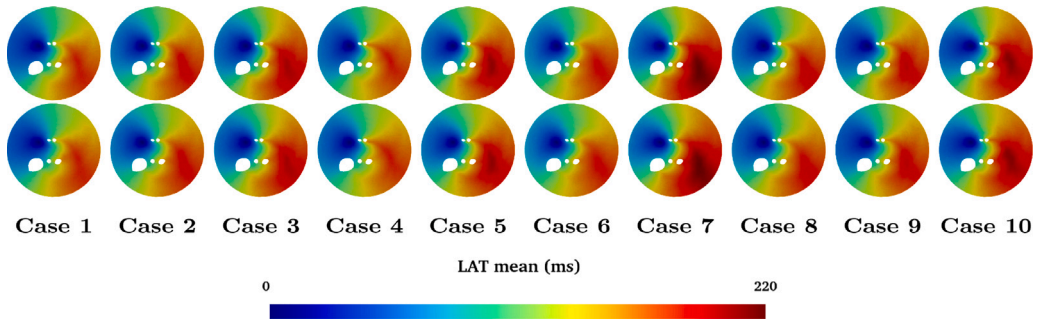

Fig. B.11. LAT mean maps computed with 12,000 MC samples (top row) and with the unscented transform (bottom row).

$[x_1, \ldots, x_{N_{pt}}, y_1, \ldots, y_{N_{pt}}, z_1, \ldots, z_{N_{pt}}]$. We assume Gaussian noise in the data, and we represent each $\mathbf{X}_{obs}$ as

$$\mathbf{X}_{obs} = \overline{\mu} + U\lambda + e_{TOT} \tag{E.1}$$

where $\overline{\mu}$ is the mean shape, U denotes the N_{modes} principal components, λ denotes the latent variables, and $e_{TOT} = e_{\perp} + e$ is the total error, consisting of the sum of the truncation error ($e_{\perp}$) and the noise (e). We

further assume that $\lambda \sim N\left(0, \Sigma_\lambda\right)$ and $e_{TOT} \sim N\left(0, \Sigma_{e_{TOT}}\right)$ and that the following expression for $\Sigma_{e_{TOT}}$ holds:

$$\Sigma_{e_{TOT}}^{i_{x_k}, j_{x_l}} = v^2 \exp\left(-\frac{d_{ij}}{l}\right)\delta_{x_k, x_l} \tag{E.2}$$

We use principal component analysis on a training set of 70 left atrium anatomies to determine $\overline{\mu}$, U, and $\sigma_i^2 = \frac{\Theta_i^2}{M-1}$ and a maximum joint
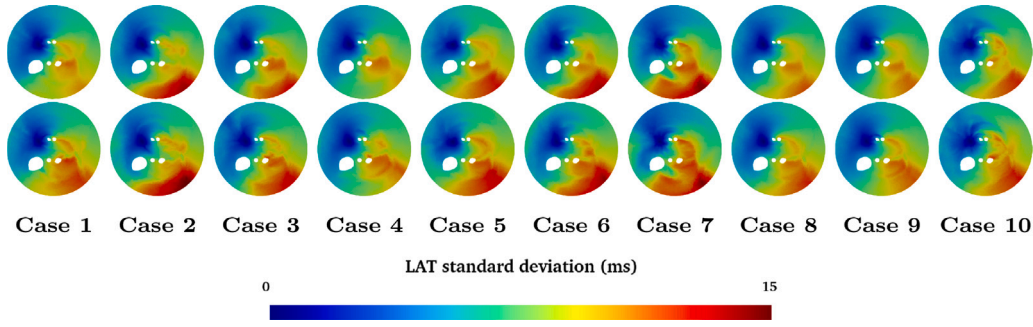
Fig. B.12. LAT standard deviation maps computed with 12,000 MC samples (top row) and with the unscented transform (bottom row).
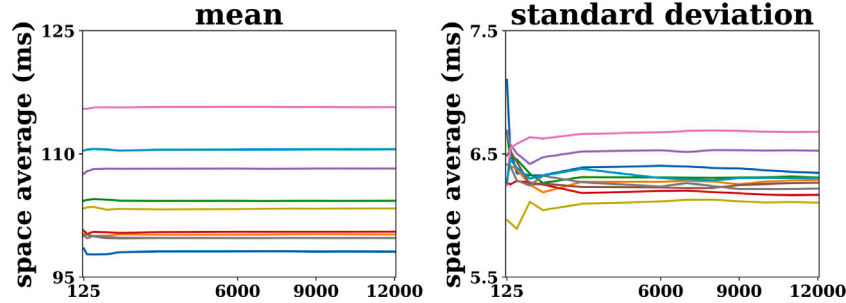

Fig. C.13. Spatial average of the sample mean LAT (left)map and of the sample standard deviation LAT map as a function of the number of samples.

Table D.4
Percentage of samples that sustained arrhythmias for each case.

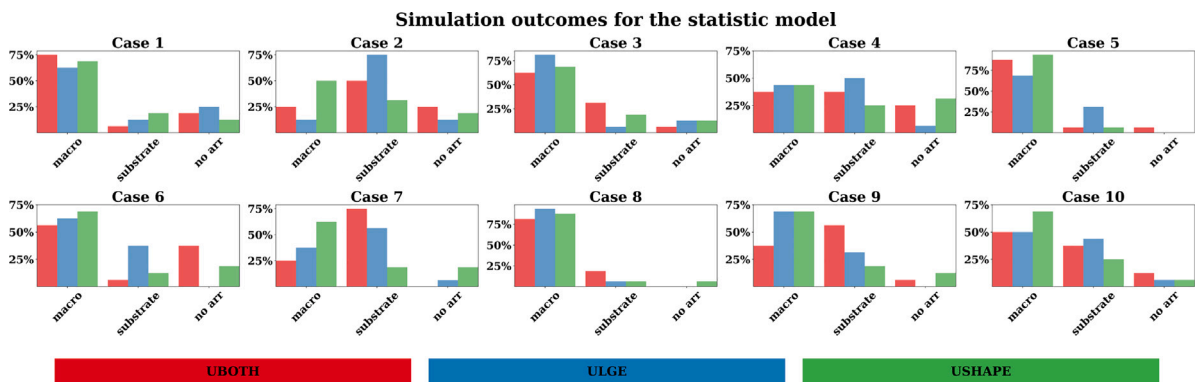| UBOTH										
Case	1	2	3	4	5	6	7	8	9	10
arr	81.25%	75%	93.75%	75%	93.75%	62.5%	100%	100%	93.75%	87.5%
no arr	18.75%	25%	6.25%	25%	6.25%	37.5%	0%	0%	6.25%	12.5%
ULGE										
Case	1	2	3	4	5	6	7	8	9	10
arr	75%	87.5%	87.5%	93.75%	100%	100%	93.75%	100%	100%	93.75%
no arr	25%	12.5%	12.5%	6.25%	0%	0%	6.25%	0%	0%	6.25%
USHAPE										
Case	1	2	3	4	5	6	7	8	9	10
arr	87.5%	81.25%	87.5%	68.75%	100%	81.25%	81.25%	93.75%	87.5%	93.75%
no arr	12.5%	18.75%	12.5%	31.25%	0%	18.75%	18.75%	6.25%	12.5%	6.25%

Fig. D.14. Percentage of samples that sustain a macro-re-entry, a substrate-driven re-entry (functional AT and AF) and that do not sustain arrhythmias, when the anatomy only (USHAPE, green), the LGE projection only (ULGE, blue), or both (UBOTH, red) produce uncertainty.

posterior estimation to estimate v^2, l. For further details, the reader is referred to [18]. For a new image $\mathbf{X}_{\text{obs}}$, we compute the posteriors

$$\Sigma_{\lambda,\text{post}} = \left(\Sigma_{\lambda}^{-1} + U^{\top} \Sigma_{e_{\text{TOT}}}^{-1} U \right)^{-1}$$

$$\boldsymbol{\mu}_{\text{post}} = \Sigma_{\lambda,\text{post}} U^{\top} \Sigma_{e_{\text{TOT}}}^{-1} (\mathbf{X}_{\text{obs}} - \overline{\mu})$$

and finally obtain:

$$\mathbf{X} \mid \mathbf{X}_{\text{obs}} \sim N \left(\overline{\mu} + U \boldsymbol{\mu}_{\text{post}}, U \Sigma_{\lambda,\text{post}} U^{\top} \right)$$

by marginalising out the dependence on λ.

Appendix F. The unscented transform

The unscented transform allows the evaluation of the output statistics of a non-linear function f when applied to an initial distribution. The unscented transform first approximates a d-dimensional probability distribution by choosing a set of points (sigma points) in the d-dimensional space, with the constraint that their moments are equal to those of the initial probability density. In this paper, we adopted spherical simplex sigma points defined in [55] and [56], choosing a null weight for the central point $W_0 = 0$, thus further reducing the set to $d + 1$ points. We further set $\alpha = \sqrt{d/(d+1)}$. We finally build the sigma-point matrix $\Xi \in \mathbb{R}^{(d+1)\times d}$ with Algorithm 1.

Algorithm 1 Generating the matrix of the sigma points

$\Xi = [\mathbf{0}]^{(d+1)\times d}$
$\alpha = \sqrt{d/(d+1)}$
$\Xi[1,1] \leftarrow -\alpha/\sqrt{2d}$
$\Xi[2,1] \leftarrow \alpha/\sqrt{2d}$
for $i \leftarrow 1$ to $(d-1)$ **do**
    for $j \leftarrow 0$ to i **do**
        $\Xi[1+j, 1+i] \leftarrow \sqrt{d/(\alpha^2(1+i)(2+i))}$
    end for
    $\Xi[2+i, 1+i] \leftarrow -(1+i)\sqrt{d/(\alpha^2(1+i)(2+i))}$
end for

For a distribution with mean $\overline{\mu}$ and covariance matrix $C = L^{\mathrm{T}}L$, the sigma points are obtained as

$$\chi_i = \overline{\mu} + L\Xi[i,:]^{\mathrm{T}}, i = 1 \ldots d+1 \tag{F.1}$$

References

[1] S.A. Niederer, K.S. Campbell, S.G. Campbell, A short history of the development of mathematical models of cardiac mechanics, J. Mol. Cell. Cardiol. 127 (2019) 11–19.

[2] C. Corrado, S. Williams, R. Karim, G. Plank, M. O'Neill, S. Niederer, A work flow to build and validate patient specific left atrium electrophysiology models from catheter measurements, Med. Image Anal. 47 (2018) 153–163.

[3] P.M. Boyle, T. Zghaib, S. Zahid, R.L. Ali, D. Deng, W.H. Franceschi, J.B. Hakim, M.J. Murphy, A. Prakosa, S. Zimmerman, H. Ashikaga, J.E. Marine, A. Kolandaivelu, S. Nazarian, D.D. Spragg, H. Calkins, N.A. Trayanova, Computationally guided personalized targeted ablation of persistent atrial fibrillation, Nat. Biomed. Eng. (2019).

[4] I.M. Khurram, R. Beinart, V. Zipunnikov, J. Dewire, H. Yarmohammadi, T. Sasaki, D.D. Spragg, J.E. Marine, R.D. Berger, H.R. Halperin, H. Calkins, S.L. Zimmerman, S. Nazarian, Magnetic resonance image intensity ratio, a normalized measure to enable interpatient comparability of left atrial fibrosis, Heart Rhythm 11 (1) (2014) 85–92.

[5] J. Siebermair, E.G. Kholmovski, N. Marrouche, Assessment of left atrial fibrosis by late gadolinium enhancement magnetic resonance imaging: Methodology and clinical implications, JACC: Clin. Electrophysiol. 3 (8) (2017) 791–802.

[6] G.R. Mirams, P. Pathmanathan, R.A. Gray, P. Challenor, R.H. Clayton, Uncertainty and variability in computational and mathematical models of cardiac physiology, J. Physiol. 594 (23) (2016) 6833–6847.

[7] R.A. Gray, P. Pathmanathan, Patient-specific cardiovascular computational modeling: Diversity of personalization and challenges, J. Cardiovasc. Transl. Res. 11 (2) (2018) 80–88.

[8] ASME V, V40, ANSI standard, assessing the credibility of computational models for medical devices, 2018, U.S. Food and Drug Administration.

[9] FDA, Assessing the credibility of computational modeling and simulation in medical device submissions, 2021, U.S. Food and Drug Administration.

[10] G. Chowdhary, R. Jategaonkar, Aerodynamic parameter estimation from flight data applying extended and unscented Kalman filter, Aerosp. Sci. Technol. 14 (2) (2010) 106–117.

[11] Z. Gao, C. Cecati, S.X. Ding, A survey of fault diagnosis and fault-tolerant techniques—Part I: Fault diagnosis with model-based and signal-based approaches, IEEE Trans. Ind. Electron. 62 (6) (2015) 3757–3767.

[12] Z. Liu, S.-C. Chan, Adaptive fading Bayesian unscented Kalman filter and smoother for state estimation of unmanned aircraft systems, IEEE Access 8 (2020) 119470–119486.

[13] S. Wang, W. Gao, A.P.S. Meliopoulos, An alternative method for power system dynamic state estimation based on unscented transform, IEEE Trans. Power Syst. 27 (2) (2012) 942–950.

[14] C. Corrado, J.-F. Gerbeau, P. Moireau, Identification of weakly coupled multiphysics problems. Application to the inverse problem of electrocardiography, J. Comput. Phys. 283 (2015) 271–298.

[15] J. Goldberger, H.K. Greenspan, J. Dreyfuss, Simplifying mixture models using the unscented transform, IEEE Trans. Pattern Anal. Mach. Intell. 30 (8) (2008) 1496–1502.

[16] S.J. Julier, J.K. Uhlmann, New extension of the Kalman filter to nonlinear systems, in: I. Kadar (Ed.), Signal Processing, Sensor Fusion, and Target Recognition VI, 3068, International Society for Optics and Photonics, SPIE, 1997, pp. 182–193.

[17] L. Angrisani, M. D'Apuzzo, R. Schiano Lo Moriello, The unscented transform: a powerful tool for measurement uncertainty evaluation, in: Proceedings of the 2005 IEEE International Workshop On Advanced Methods for Uncertainty Estimation in Measurement, 2005, pp. 27–32.

[18] C. Corrado, O. Razeghi, C. Roney, S. Coveney, S. Williams, I. Sim, M. O'Neill, R. Wilkinson, J. Oakley, R.H. Clayton, S. Niederer, Quantifying atrial anatomy uncertainty from clinical data and its impact on electro-physiology simulation predictions, Med. Image Anal. 61 (2020) 101626.

[19] C.H. Roney, C. Sillett, J. Whitaker, J.A.S. Lemus, I. Sim, I. Kotadia, M. O'Neill, S.E. Williams, S.A. Niederer, Applications of multimodality imaging for left atrial catheter ablation, Eur. Heart J. - Cardiovasc. Imaging (2021).

[20] S. Zahid, K.N. Whyte, E.L. Schwarz, R.C. Blake, P.M. Boyle, J. Chrispin, A. Prakosa, E.G. Ipek, F. Pashakhanloo, H.R. Halperin, H. Calkins, R.D. Berger, S. Nazarian, N.A. Trayanova, Feasibility of using patient-specific models and the "minimum cut" algorithm to predict optimal ablation targets for left atrial flutter, Heart Rhythm 13 (8) (2016) 1687–1698.

[21] G. Caixal, F. Alarcón, T.F. Althoff, M. Nuñez-Garcia, E.M. Benito, R. Borràs, R.J. Perea, S. Prat-González, P. Garre, D. Soto-Iglesias, C. Gunturitz, J. Cozzari, M. Linhart, J.M. Tolosana, E. Arbelo, I. Roca-Luque, M. Sitges, E. Guasch, L. Mont, Accuracy of left atrial fibrosis detection with cardiac magnetic resonance: correlation of late gadolinium enhancement with endocardial voltage and conduction velocity, EP Europace 23 (3) (2020) 380–388.

[22] C. Corrado, N. Zemzemi, A conduction velocity adapted eikonal model for electrophysiology problems with re-excitability evaluation, Med. Image Anal. 43 (2018) 186–197.

[23] O. Razeghi, I. Sim, C.H. Roney, R. Karim, H. Chubb, J. Whitaker, L. O'Neill, R. Mukherjee, M. Wright, M. O'Neill, S.E. Williams, S. Niederer, Fully automatic atrial fibrosis assessment using a multilabel convolutional neural network, Circulation: Cardiovascular Imaging 13 (12) (2020) e011512.

[24] O. Razeghi, J.A. Solís-Lemus, A.W. Lee, R. Karim, C. Corrado, C.H. Roney, A. de Vecchi, S.A. Niederer, CemrgApp: An interactive medical imaging application with image processing, computer vision, and machine learning toolkits for cardiovascular research, SoftwareX 12 (2020) 100570.

[25] S. Durrleman, M. Prastawa, N. Charon, J.R. Korenberg, S. Joshi, G. Gerig, A. Trouvé, Morphometry of anatomical shape complexes with dense deformations and sparse parameters, NeuroImage 101 (2014) 35–49.

[26] S. Zahid, H. Cochet, P.M. Boyle, E.L. Schwarz, K.N. Whyte, E.J. Vigmond, R. Dubois, M. Hocini, M. Haïssaguerre, P. Jaïs, N.A. Trayanova, Patient-derived models link re-entrant driver localization in atrial fibrillation to fibrosis spatial pattern, Cardiovasc. Res. 110 (3) (2016) 443–454.

[27] M. Courtemanche, R.J. Ramirez, S. Nattel, Ionic mechanisms underlying human atrial action potential properties: insights from a mathematical model, Am. J. Physio.-Heart and Circulatory Physiol. 275 (1) (1998) H301–H321, http://dx.doi.org/10.1152/ajpheart.1998.275.1.H301.

[28] K.T. Konings, C.J. Kirchhof, J.R. Smeets, H.J. Wellens, O.C. Penn, M.A. Allessie, High-density mapping of electrically induced atrial fibrillation in humans, Circulation 89 (4) (1994) 1665–1680, https://www.ahajournals.org/doi/pdf/10.1161/01.CIR.89.4.1665.

[29] D.M. Pedrotty, R.Y. Klinger, R.D. Kirkton, N. Bursac, Cardiac fibroblast paracrine factors alter impulse conduction and ion channel expression of neonatal rat cardiomyocytes, Cardiovasc. Res. 83 (4) (2009) 688–697, https://academic.oup.com/cardiovascres/article-pdf/83/4/688/17198339/cvp164.pdf.

[30] D. Li, S. Fareh, T.K. Leung, S. Nattel, Promotion of atrial fibrillation by heart failure in dogs, Circulation 100 (1) (1999) 87–95, https://www.ahajournals.org/doi/pdf/10.1161/01.CIR.100.1.87.

[31] B. Burstein, P. Comtois, G. Michael, K. Nishida, L. Villeneuve, Y.-H. Yeh, S. Nattel, Changes in connexin expression and the atrial fibrillation substrate in congestive heart failure, Circ. Res. 105 (12) (2009) 1213–1222, https://www.ahajournals.org/doi/pdf/10.1161/CIRCRESAHA.108.183400.

[32] R. Karim, Y. Ma, M. Jang, R.J. Housden, S.E. Williams, Z. Chen, A. Ataollahi, K. Althoefer, C.A. Rinaldi, R. Razavi, M.D. O'Neill, T. Schaeffter, K.S. Rhode, Surface flattening of the human left atrium and proof-of-concept clinical applications, Comput. Med. Imaging Graph. 38 (4) (2014) 251–266.

[33] J.D. Bayer, C.H. Roney, A. Pashaei, P. Jaïs, E.J. Vigmond, Novel radiofrequency ablation strategies for terminating atrial fibrillation in the left atrium: A simulation study, Front. Physiol. 7 (2016).

[34] X. Li, C.H. Roney, B.S. Handa, R.A. Chowdhury, S.A. Niederer, N.S. Peters, F.S. Ng, Standardised framework for quantitative analysis of fibrillation dynamics, Sci. Rep. 9 (1) (2019) 16671.

[35] S.M. Narayan, D.E. Krummen, K. Shivkumar, P. Clopton, W.-J. Rappel, J.M. Miller, Treatment of atrial fibrillation by the ablation of localized sources: CONFIRM (Conventional Ablation for Atrial Fibrillation With or Without Focal Impulse and Rotor Modulation) trial, J. Am. Coll. Cardiol. 60 (7) (2012) 628–636.

[36] R.A. Winkle, R. Moskovitz, R.H. Mead, G. Engel, M.H. Kong, W. Fleming, R.A. Patrawala, Ablation of atypical atrial flutters using ultra-high density-activation sequence mapping, J. Interv. Cardiac Electrophysiol. 48 (2) (2017) 177–184.

[37] C. Corrado, S.A. Niederer, A two-variable model robust to pacemaker behaviour for the dynamics of the cardiac action potential, Math. Biosci. 281 (2016) 46–54.

[38] E.T. Bieging, A. Morris, B.D. Wilson, C.J. McGann, N.F. Marrouche, J. Cates, Left atrial shape predicts recurrence after atrial fibrillation catheter ablation, J. Cardiovasc. Electrophysiol. 29 (7) (2018) 966–972.

[39] C. Prieto, M. Doneva, M. Usman, M. Henningsson, G. Greil, T. Schaeffter, R.M. Botnar, Highly efficient respiratory motion compensated free-breathing coronary mra using golden-step cartesian acquisition, J. Magn. Reson. Imag. 41 (3) (2015) 738–746.

[40] J. Heijman, H. Sutanto, H.J.G.M. Crijns, S. Nattel, N.A. Trayanova, Computational models of atrial fibrillation: achievements, challenges, and perspectives for improving clinical care, Cardiovasc. Res. 117 (7) (2021) 1682–1699.

[41] A. Loewe, E. Poremba, T. Oesterlein, A. Luik, C. Schmitt, G. Seemann, O. Dössel, Patient-specific identification of atrial flutter vulnerability–A computational approach to reveal latent reentry pathways, Front. Physiol. 9 (2019).

[42] N. Vandersickel, E. Van Nieuwenhuyse, N. Van Cleemput, J. Goedgebeur, M. El Haddad, J. De Neve, A. Demolder, T. Strisciuglio, M. Duytschaever, A.V. Panfilov, Directed networks as a novel way to describe and analyze cardiac excitation: Directed graph mapping, Front. Physiol. 10 (2019).

[43] S. Coveney, C. Corrado, C.H. Roney, R.D. Wilkinson, J.E. Oakley, F. Lindgren, S.E. Williams, M.D. O'Neill, S.A. Niederer, R.H. Clayton, Probabilistic interpolation of uncertain local activation times on human atrial manifolds, IEEE Trans. Biomed. Eng. 67 (1) (2020) 99–109.

[44] C.L. Lei, S. Ghosh, D.G. Whittaker, Y. Aboelkassem, K.A. Beattie, C.D. Cantwell, T. Delhaas, C. Houston, G.M. Novaes, A.V. Panfilov, P. Pathmanathan, M. Riabiz, R.W. dos Santos, J. Walmsley, K. Worden, G.R. Mirams, R.D. Wilkinson, Considering discrepancy when calibrating a mechanistic electrophysiology model, Phil. Trans. R. Soc. A 378 (2173) (2020) 20190349.

[45] A. Muszkiewicz, X. Liu, A. Bueno-Orovio, B.A.J. Lawson, K. Burrage, B. Casadei, B. Rodriguez, From ionic to cellular variability in human atrial myocytes: an integrative computational and experimental study, Am. J. Physiol.-Heart and Circ. Physiol. 314 (5) (2018) H895–H916.

[46] N. van Osta, F.P. Kirkels, T. van Loon, T. Koopsen, A. Lyon, R. Meiburg, W. Huberts, M.J. Cramer, T. Delhaas, K.H. Haugaa, A.J. Teske, J. Lumens, Uncertainty quantification of regional cardiac tissue properties in arrhythmogenic cardiomyopathy using adaptive multiple importance sampling, Front. Physiol. 12 (2021).

[47] C. Rodero, M. Strocchi, M. Marciniak, S. Longobardi, J. Whitaker, M.D. O'Neill, K. Gillette, C. Augustin, G. Plank, E.J. Vigmond, P. Lamata, S.A. Niederer, Linking statistical shape models and simulated function in the healthy adult human heart, PLoS Comput. Biol. 17 (4) (2021) 1–28.

[48] Z. Hu, D. Du, Y. Du, Generalized polynomial chaos-based uncertainty quantification and propagation in multi-scale modeling of cardiac electrophysiology, Comput. Biol. Med. 102 (2018) 57–74.

[49] H. Chubb, S. Aziz, R. Karim, C. Sohns, O. Razeghi, S.E. Williams, J. Whitaker, J. Harrison, A. Chiribiri, T. Schaeffter, M. Wright, M. O'Neill, R. Razavi, Optimization of late gadolinium enhancement cardiovascular magnetic resonance imaging of post-ablation atrial scar: a cross-over study, J. Cardiovasc. Magn. Reson. 20 (1) (2018) 30.

[50] C. Reiter, U. Reiter, C. Kräuter, V. Nizhnikava, A. Greiser, D. Scherr, A. Schmidt, M. Fuchsjäger, G. Reiter, Differences in left ventricular and left atrial function assessed during breath-holding and breathing, Eur. J. Radiol. 141 (2021) 109756.

[51] Y.-C. Liao, J.-N. Liao, L.-W. Lo, Y.-J. Lin, S.-L. Chang, Y.-F. Hu, T.-F. Chao, F.-P. Chung, T.-C. Tuan, A.L.D. Te, R. Walia, S. Yamada, C.-H. Lin, C.-Y. Lin, Y.-T. Chang, S. Allamsetty, W.-C. Yu, J.-L. Huang, T.-J. Wu, S.-A. Chen, Left atrial size and left ventricular end-systolic dimension predict the progression of paroxysmal atrial fibrillation after catheter ablation, J. Cardiovasc. Electrophysiol. 28 (1) (2017) 23–30.

[52] A. Njoku, M. Kannabhiran, R. Arora, P. Reddy, R. Gopinathannair, D. Lakkireddy, P. Dominic, Left atrial volume predicts atrial fibrillation recurrence after radiofrequency ablation: a meta-analysis, EP Europace 20 (1) (2017) 33–42.

[53] D. Deng, M.J. Murphy, J.B. Hakim, W.H. Franceschi, S. Zahid, F. Pashakhanloo, N.A. Trayanova, P.M. Boyle, Sensitivity of reentrant driver localization to electrophysiological parameter variability in image-based computational models of persistent atrial fibrillation sustained by a fibrotic substrate, Chaos 27 (9) (2017) 093932.

[54] A. Kaboudian, H.A. Velasco-Perez, S. Iravanian, Y. Shiferaw, E.M. Cherry, F.H. Fenton, A comprehensive comparison of GPU implementations of cardiac electrophysiology models, in: E. Bartocci, R. Cleaveland, R. Grosu, O. Sokolsky (Eds.), From Reactive Systems To Cyber-Physical Systems: Essays Dedicated To Scott a. Smolka on the Occasion of His 65th Birthday, Springer International Publishing, 2019, pp. 9–34.

[55] K.G. Papakonstantinou, M. Amir, G.P. Warn, A Scaled Spherical Simplex Filter (S3F) with a decreased n + 2 sigma points set size and equivalent 2n + 1 Unscented Kalman Filter (UKF) accuracy, Mech. Syst. Signal Process. 163 (2022) 107433.

[56] J.G. Castrejon Lozano, L.R. Garca Carrillo, A. Dzul, R. Lozano, Spherical simplex sigma-point Kalman filters: A comparison in the inertial navigation of a terrestrial vehicle, in: 2008 American Control Conference, 2008, pp. 3536–3541.